PHYSICAL REVIEW B **107**, 104412 (2023)

Magnetic structure and crystal field states of $Pr_2Pd_3Ge_5$: μSR and neutron scattering investigations

V. K. Anand,[1,2,*] D. T. Adroja,[1,3,†] C. Ritter,[4] Debarchan Das,[5] Harikrishnan S. Nair,[6] A. Bhattacharyya,[1,7]
Leandro Liborio,[8] Simone Sturniolo,[8] F. L. Pratt,[1] Duc Le,[1] G. Andre,[9] Hubertus Luetkens,[5]
A. D. Hillier,[1] and Z. Hossain[10]

[1]*ISIS Facility, Rutherford Appleton Laboratory, Chilton, Didcot, Oxon, OX11 0QX, United Kingdom*
[2]*Department of Physics, University of Petroleum and Energy Studies, Dehradun, Uttarakhand 248007, India*
[3]*Highly Correlated Matter Research Group, Physics Department, University of Johannesburg,*
P.O. Box 524, Auckland Park 2006, South Africa
[4]*Institut Laue-Langevin, Boite Postale 156, 38042 Grenoble Cedex, France*
[5]*Laboratory for Muon Spin Spectroscopy, Paul Scherrer Institute, CH-5232 Villigen PSI, Switzerland*
[6]*Department of Physics, University of Texas at El Paso, 500 W. University Ave, El Paso, Texas 79968, USA*
[7]*Department of Physics, Ramakrishna Mission Vivekananda Educational and Research Institute, Howrah 711202, India*
[8]*Scientific Computing Department, Rutherford Appleton Laboratory, Chilton, Didcot, Oxon, OX11 0QX, United Kingdom*
[9]*Laboratoire Leon Brillouin (CEA-CNRS), CEA/Saclay, F-91191 Gif-sur-Yvette, France*
[10]*Department of Physics, Indian Institute of Technology, Kanpur 208016, India*

(Received 14 November 2022; accepted 23 February 2023; published 14 March 2023)

We present the results of muon spin relaxation (μSR), neutron powder diffration (NPD), and inelastic neutron scattering (INS) investigations on polycrystalline $Pr_2Pd_3Ge_5$. The polycrystalline $Pr_2Pd_3Ge_5$ is known to exhibit two antiferromagnetic transitions near $T_{N1} = 8.3$ K and $T_{N2} = 7.5$ K which is confirmed by the heat capacity measurements on the present sample. In the magnetically ordered state the NPD data show clear evidence for magnetic Bragg peaks, which for $T < T_{N2}$ could be indexed with a propagation vector $\mathbf{k} = (1, 0, 0)$, and with $\mathbf{k} = (1, 0, 0.07)$ for $T_{N2} < T < T_{N1}$. We have determined the magnetic structure and found a canted antiferromagnetic structure of ordered Pr^{3+} moments. At 7.6 K we find an amplitude modulated incommensurate antiferromagnetic arrangement of ordered moments with a maximum ordered moment of 1.64(3) μ_B/Pr lying in the *ab* plane tilted at about 26° from the *b* axis. At 1.8 K the antiferromagnetic structure is found to be commensurate with an ordered moment of 2.80(6) μ_B/Pr lying in the *ab* plane tilted at about 28° from the *b* axis. Our zero-field μSR spectra at 1.5 K and at shorter time scale (below 0.5 µs) reveal two oscillatory frequencies further supporting a long-range-ordered magnetic ground state. We have calculated the muon sites using the density functional theory calculation and present the results of internal field calculations at the muon stopping sites, which are in good agreement with the experimental observations. In the paramagnetic state, the INS data show three well defined CEF excitations near 8.0, 12.3, and 18.1 meV arising from the crystal electric field (CEF) split $J = 4$ ground state of Pr^{3+}. The CEF level scheme is deduced by analyzing the INS data by a model based on the CEF model.

DOI: 10.1103/PhysRevB.107.104412

I. INTRODUCTION

The rare earth intermetalllic compounds present a variety of magnetic ground states determined by competing Rudderman-Kittel-Kasuya-Yosida interaction, the Kondo interaction and crystal electric field (CEF) effect. Among the rare earths, Pr-based compounds with Pr^{3+} ($J = 4$) present interesting magnetic ground states because of the action of the CEF that can split the nine-fold degenerate ground state multiplet into a combination of singlet, doublet, and/or triplet states depending on the symmetry of the crystallographic environment. Usually a Pr compound with a CEF-split singlet as ground state does not order magnetically [1]. In a singlet ground state system an induced-moment magnetic ordering may occur provided the relative strength of the exchange interaction J_{ex} among the Pr^{3+} ions and the CEF splitting energy Δ (between the ground state and the first excited state) exceeds a certain critical value [2,3]. The well known examples of Pr-based CEF-split singlet ground state systems exhibiting the induced-moment spontaneous ordering are Pr_3Tl, Pr_3In and $PrRu_2Si_2$ [4–11]. Recently, we found evidence for induced-moment magnetism in singlet ground state system $PrIrSi_3$ [12], whereas no evidence for induced-moment magnetic ordering was observed in the singlet ground state system $PrRhSi_3$ [13].

An interesting competition between the CEF splitting and exchange interaction is observed in the induced-moment singlet system that can lead to a spin-glass-type behavior in

---

[*] vivekkranand@gmail.com

[†] devashibhai.adroja@stfc.ac.uk

a crystallographically well-ordered stoichiometric Pr compound such as in $PrAu_2Si_2$ [14,15]. For $PrAu_2Si_2$ there is no obvious source of geometric frustration or site disorder which are the usual route to spin-glass behavior. Goremychkin *et al.* [15] proposed a novel mechanism based on the dynamic fluctuations of the CEF levels to explain the spin-glass behavior in stoichiometric $PrAu_2Si_2$. In this singlet ground state system the ratio J_{ex}/Δ meets the requirement of induced moment magnetic ordering, however, the exchange coupling is very close to the critical value required to induce the magnetic order, therefore the dynamic fluctuations of the crystal field levels can destabilize the induced moment long-range magnetic order resulting in a frustrated ground state, i.e., spin-glass type behavior. The mechanism based on dynamic fluctuations of CEF levels is also believed to be the origin of spin-glass behavior in $PrRuSi_3$ [16], $PrRhSn_3$ [17] and $PrIr_2B_2$ [18].

Excitonic mass enhancement by low-lying crystal field excitations is another striking behavior that leads to the development of the heavy fermion state in a Pr-based singlet ground state system. In superconducting $PrOs_4Sb_{12}$ [19,20] the formation of a heavy-fermion state through this peculiar mechanism, produced by the electronic scattering with the crystalline electric field levels, is quite distinct from the usual Kondo route to heavy fermions in Ce/Yb-compounds. Excitonic mass enhancement by the low-lying crystal field excitations is also believed to be at the origin of the heavy fermion behavior in the singlet ground state system $PrRh_2B_2C$ [21] and of the moderate heavy fermion behavior in the singlet ground state system $Pr_2Rh_3Ge_5$ [22].

The doublet ground state system $Pr_2Pd_3Ge_5$, which is being investigated by muon spin relaxation (μSR) and neutron scattering in the present work, exhibits two antiferromagnetic transitions near $T_{N1} = 8.3$ K and $T_{N2} = 7.5$ K in polycrystalline form as inferred from the magnetic susceptibility $\chi(T)$ and heat capacity $C_p(T)$ data [22]. In the ordered state the isothermal magnetization $M(H)$ exhibits a field-induced metamagnetic transition, at $H \sim 1.6$ T at 2 K. The electrical resistivity $\rho(H)$ reveals an anomalously high positive magnetoresistance ($\sim$900 % at 2 K and 10 T) [22]. Both $\rho(T)$ and $C_p(T)$ show gapped magnon behavior at $T < T_{N2}$ with an energy gap of $\sim$0.25 meV [22]. A complex and highly anisotropic magnetic behavior is inferred from the magnetic measurements on single crystal $Pr_2Pd_3Ge_5$ [23]. The $\chi(T)$ data of single crystal $Pr_2Pd_3Ge_5$ exhibit four magnetic transitions at 8.0, 7.3, 6.2, and 4.9 K for $H \parallel a$ and $H \parallel b$, and two transitions at 6.9 and 6.3 K for $H \parallel c$ [23]. The H-T phase diagram presents three magnetic phases for $H \parallel a$ and $H \parallel b$, whereas there are two magnetic phases for $H \parallel c$ [23]. The $M(H)$ isotherms reveal multiple field-induced metamagnetic transitions and the $\rho(T)$ data show the signature of super-zone gap formation and hence possible incommensurate antiferromagnetic structure in this compound [23].

Continuing our efforts to explore the novel magnetic ground state of $Pr_2T_3X_5$ (T = Ni, Co, Pd, Pt, Rh, and X = Si, Ge) compounds [22–27], here we report the results of μSR, neutron powder diffraction (NPD), and inelastic neutron scattering (INS) measurements on polycrystalline $Pr_2Pd_3Ge_5$. The ac susceptibility data reveal two transitions at $T_{N1} = 8.25$ K and $T_{N2} = 7.5$ K as previously found for polycrystalline $Pr_2Pd_3Ge_5$ [22]. The heat capacity measurement also confirms two transitions associated with antiferromagnetic transitions at T_{N1} and T_{N2}. The long-range antiferromagnetic ordering is further confirmed by neutron diffraction which shows clear evidence for magnetic Bragg peaks, indexed by the propagation vector $\mathbf{k} = (1, 0, 0)$ between 1.5 and 7.5 K and by $\mathbf{k} = (1, 0, 0.07)$ at 7.6 K. The magnetic structure is found to be a canted antiferromagnet with an ordered magnetic moment of $2.80(6)\,\mu_B/\mathrm{Pr}$ at 1.8 K (equal moment, commensurate), and an amplitude modulated structure at 7.6 K (sine wave, incommensurate). The μSR data show oscillatory asymmetry having two frequencies at 1.5 K, and with increasing temperature the higher frequency nearly disappears above 5 K. The INS data provide information about the CEF level scheme by probing the CEF excitations from Pr^{3+} ions.

II. EXPERIMENTAL DETAILS

The polycrystalline sample of $Pr_2Pd_3Ge_5$ was prepared by arc-melting the stoichiometric mixture of high purity elements (Pr: 99.9%, Pd: 99.99%, and Ge: 99.99%) on a water-cooled copper hearth under a high purity inert argon atmosphere. The arc-melted button was flipped and remelted several times to ensure homogeneity. In order to improve the phase formation, the arc-melted button was annealed at 1000 °C for a week. We also prepared $La_2Rh_3Ge_5$ using the same method as above which was used as a phonon reference for $Pr_2Pd_3Ge_5$ in our inelastic neutron scattering study. The phase purity and crystal structure was checked by powder x-ray diffraction which revealed the samples to be single phase. The ac magnetic susceptibility and heat capacity were measured using a Quantum Design Physical Properties Measurement System. The μSR measurements were carried out using the GPS spectrometer at the πM3.2 beamline at the Swiss Muon Source of the Paul Scherrer Institut. The measurements down to 1.5 K were carried out on the pressed powdered pellet (diameter 7 mm) of $Pr_2Pd_3Ge_5$ which was then mounted on a Cu holder using GE varnish. This sample holder assembly was then mounted into a He-flow cryostat. Positively charged spin polarized muons (momentum 28 MeV/c) were implanted into the sample and the positrons from the muon decay were registered in up and down detectors. The μSR spectra were analyzed using the MUSRFIT software package [28].

The NPD measurements were carried out using the G 4-1 two-axis powder diffractometer equipped with a vertical focusing pyrolytic graphite monochromator at Laboratoire Léon Brillouin (LLB), Saclay, France. The $Pr_2Pd_3Ge_5$ sample was powdered and lightly packed in a thin-walled vanadium can (diameter 6 mm). The sample mount was cooled down to 1.5 K inside a He-4 cryostat using He-exchange gas. NPD data were collected using $\lambda = 2.423$ Å with a typical counting of 4 h per run at several temperatures below 10 K.

The INS measurements were carried out using the time-of-flight spectrometer MARI at the ISIS Facility, UK. The powdered $Pr_2Pd_3Ge_5$ (mass 11 g) was mounted by wrapping the sample in a thin Al-foil which was fixed inside a thin walled Al can. The sample-mount was cooled down to 5 K using a top-loading closed-cycle refrigerator with He-exchange gas. The INS data were collected with neutrons of incident energies $E_i = 6$, 20, 30, and 40 meV and scattering angle 3°

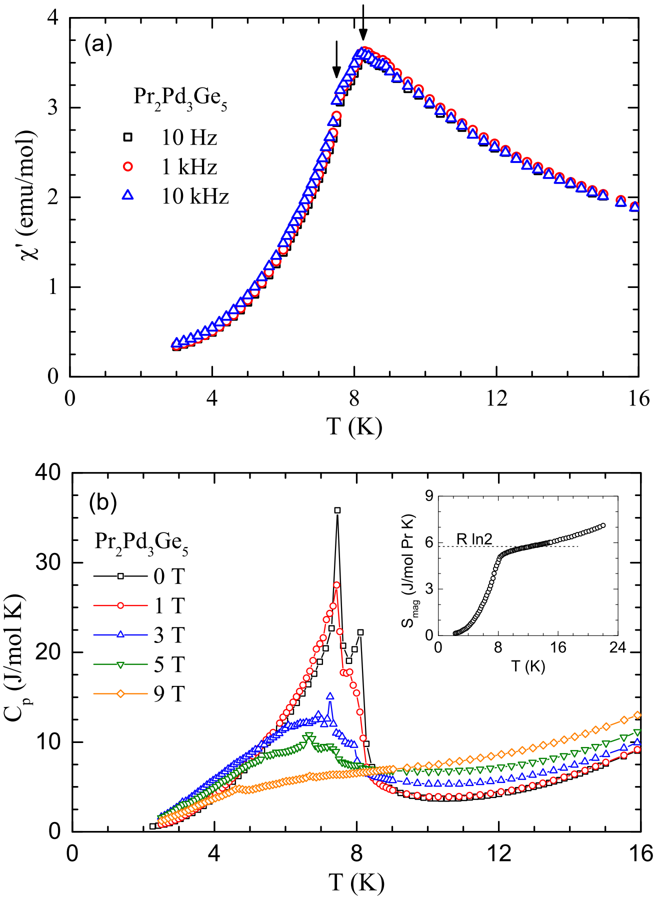

FIG. 1. (a) Temperature T dependence of real part χ' of the ac magnetic susceptibility χ_{ac} of $Pr_2Pd_3Ge_5$ measured at frequencies 10 Hz, 1 kHz and 10 kHz in an applied ac magnetic field of 1.0 mT. (b) T dependence of heat capacity C_p of $Pr_2Pd_3Ge_5$ measured at different H for $0 \leqslant H \leqslant 9$ T. Inset: T dependence of magnetic entropy S_{mag}.

and 134°. Additional INS measurements were also carried out using the 4F1, cold neutron three-axis spectrometer at LLB, France between 3.8 and 78 K using an orange He-4 cryostat. The INS data were collected using a PG002 analyzer with final wave vector fixed at $\mathbf{k}_F = 1.550$ Å^{-1}.

III. RESULTS AND DISCUSSION

A. ac susceptibility and heat capacity

Figure 1(a) shows the temperature T dependence of the real part χ' of the ac susceptibility χ_{ac} of $Pr_2Pd_3Ge_5$ for three representative frequencies 10 Hz, 1 kHz, and 10 kHz measured with an ac magnetic field of 1.0 mT. As marked by arrows in Fig. 1(a), we see two anomalies near $T_{N1} = 8.25$ K and $T_{N2} = 7.5$ K in $\chi'(T)$ consistent with the anomalies seen in dc magnetic susceptibility and heat capacity of polycrystalline $Pr_2Pd_3Ge_5$ [22]. As is expected for an antiferromagnetic ordering, no frequency dependence is noticed for either 8.25 or 7.5 K anomalies over the entire range of measured frequency 10 Hz $\leqslant \nu \leqslant$ 10 kHz. The imaginary part $\chi''(T)$ also displays the corresponding anomalies (data not shown).

Figure 1(b) shows the T dependence of the heat capacity of $Pr_2Pd_3Ge_5$ measured in zero field as well as under applied fields, $0 \leqslant H \leqslant 9$ T. Two sharp λ-type anomalies in $C_p(T)$ measured in $H = 0$ clearly evidence the two magnetic transitions at T_{N1} and T_{N2}. With the application of magnetic field peak heights reduce and the peak positions shift to lower temperatures, e.g., at $H = 5$ T the two anomalies associated with T_{N1} and T_{N2} move to 7.4 and 6.6 K, respectively. At 9 T the first anomaly is nearly smoothened but a second anomaly is seen near 4.6 K. The shift of the peak positions to lower temperatures with applied fields indicates an antiferromagnetic ground state. As can be seen from the inset of Fig. 1(b), the magnetic entropy $S_{mag}(T)$ attains a value of about 90% of $R \ln 2$ at T_{N1} which indicates a doublet CEF ground state of the Pr^{3+} ion. However, for an orthorhombic environment the ninefold degenerate ground state of Pr^{3+} ion is expected to split in nine singlets, therefore the inference of a doublet ground state can be interpreted as a quasidoublet state consisting of two closely situated singlets. Indeed, the CEF level scheme deduced from the analysis of inelastic neutron scattering data (Sec. III D) reveals two singlets at 0 and 0.3 meV which behave like a quasidoublet state.

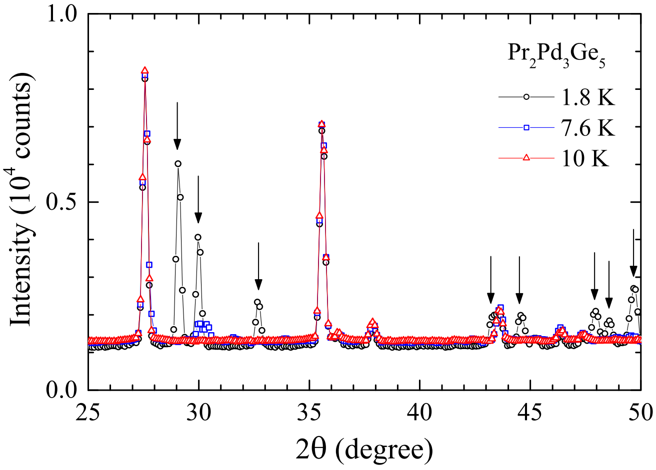

FIG. 2. A comparison of neutron diffraction patterns of $Pr_2Pd_3Ge_5$ recorded at 10 K (above T_{N1}), 7.6 K (between T_{N1} and T_{N2}) and 1.8 K (below T_{N2}). The magnetic Bragg peaks appearing at 1.8 K are marked with arrows.

B. Neutron powder diffraction

Figures 2 and 3 show the neutron diffraction data collected on the powdered $Pr_2Pd_3Ge_5$ sample, displaying the patterns for three representative temperatures 10 K ($T > T_{N1}$), 7.6 K ($T_{N2} < T < T_{N1}$) and 1.8 K ($T < T_{N2}$). The comparison of NPD patterns shown in Fig. 2 clearly displays the appearance of additional reflections of magnetic origin at 7.6 and 1.8 K. The magnetic Bragg peaks appearing at 1.8 K are marked with arrows in Fig. 2.

The NPD data at 10 K could be successfully refined with the $U_2Co_3Si_5$-type orthorhombic (space group *Ibam*) structural model. The FULLPROF [29] structural refinement profile is shown in Fig. 3(a) and crystallographic parameters are listed in Table I. On the other hand, the NPD patterns at 7.6 and 1.8 K were analyzed using the crystal structure and magnetic structure refinements. First we discuss the steps involved in refinement of 1.8 K data. The magnetic propagation

TABLE I. Refined crystallographic parameters obtained from the structural Rietveld refinement of neutron powder diffraction data of $Pr_2Pd_3Ge_5$ at 10 K.

Structure	$U_2Co_3Si_5$-type orthorhombic
Space group	*Ibam* (No. 72)
Lattice parameters	
a (Å)	10.1638(5)
b (Å)	12.0517(5)
c (Å)	6.1522(3)
V_{cell} (Å^3)	753.58(6)
Atomic coordinates	

Atom	Wyckoff position	x	y	z
Pr	$8j$	0.266(2)	0.122(3)	0
Pd1	$4a$	0	0	1/4
Pd2	$8j$	0.1047(7)	0.361(2)	0
Ge1	$4b$	1/2	0	1/4
Ge2	$8g$	0	0.2256(7)	1/4
Ge3	$8j$	0.3450(6)	0.392(1)	0

vector **k** was determined using the program k-search of the FULLPROF suite providing a direct estimation of a commensurate propagation vector $\mathbf{k} = (1, 0, 0)$. This propagation vector has also been found to index the magnetic Bragg peaks in antiferromagnetic $Ce_2Ni_3Ge_5$ [30,31]. The symmetry analysis for the propagation vector $\mathbf{k} = (1, 0, 0)$ and space group *Ibam* using the program BASIREPS [32,33] suite yielded eight nonzero irreducible representations (IRs) for the magnetic Pr($8j$) site: one-dimensional representations Γ_1^1, Γ_2^1, Γ_3^1, Γ_4^1, Γ_5^1, Γ_6^1, Γ_7^1, and Γ_8^1 in the little group. The magnetic representation consisting of eight IRs is $\Gamma_{\mathrm{mag\,Pr}} = 1\,\Gamma_1^1 + 2\,\Gamma_2^1 + 1\,\Gamma_3^1 + 2\,\Gamma_4^1 + 2\,\Gamma_5^1 + 1\,\Gamma_6^1 + 2\,\Gamma_7^1 + 1\,\Gamma_8^1$.

Out of these eight IRs, the best refinement of the magnetic diffraction pattern at 1.8 K, is obtained for IR Γ_4^1 (with magnetic R factor of 7.51%) which has two basis functions. The structural and magnetic refinement profile of the NPD pattern at 1.8 K is shown in Fig. 3(c). The magnetic structure obtained from the refinement is shown in Fig. 4(a). The magnetic structure at 1.8 K is found to be a canted antiferromagnet with ordered moments lying in the *ab* plane tilted about 28° from the b axis. In the a direction the moments are coupled as $+-+-$ and in the b direction as $+--+$. The ordered moment is found to be $m = 2.80(6)\,\mu_B/\mathrm{Pr}$ with a component $m_a = 1.31(5)\,\mu_B/\mathrm{Pr}$ and b component $m_b = 2.47(4)\,\mu_B/\mathrm{Pr}$. A canted antiferromagnetic structure has also been inferred in the case of $Ce_2Ni_3Ge_5$ through the neutron diffraction measurement on a single crystal sample [31].

At 7.6 K the magnetic Bragg peaks could not be indexed with the propagation vector $\mathbf{k} = (1, 0, 0)$, instead we find an incommensurate propagation vector $\mathbf{k} = (1, 0, 0.070(1))$ to be the best solution. The symmetry analysis for $\mathbf{k} = (1, 0, 0.07)$ yielded four nonzero IRs for the magnetic Pr($8j$) site: one-dimensional representations Γ_1^1, Γ_2^1, Γ_3^1, and Γ_4^1 in the little group, such that the magnetic representation $\Gamma_{\mathrm{mag\,Pr}} = 3\,\Gamma_1^1 + 3\,\Gamma_2^1 + 3\,\Gamma_3^1 + 3\,\Gamma_4^1$. The IR Γ_1^1 which has three basis functions provides the best refinement of the magnetic diffraction pattern at 7.6 K. The structural and magnetic refinement profile for the NPD pattern at 7.6 K is shown in Fig. 3(b), and the magnetic refinement of the temperature difference data set (7.6 −10 K) which contains only the magnetic diffraction intensity is shown in Fig. 3(d). The magnetic structure obtained from the refinement is shown in Fig. 4(b). The magnetic structure is found to be an amplitude modulated incommensurate antiferromagnetic structure with the ordered moments lying in the *ab* plane tilted about 26° from the b axis. The magnetic coupling at 7.6 K is same as at 1.8 K. The maximum amplitude of the sine wave modulated ordered moment is found to be $m = 1.64(3)\,\mu_B/\mathrm{Pr}$. The finding of an incommensurate antiferromagnetic structure below T_{N1} is consistent with the indication of super-zone gap formation in the resistivity measurement on single crystal $Pr_2Pd_3Ge_5$ [23].

The T dependence of the ordered moment m which was obtained from the refinement of NPD patterns at different temperatures is shown in Fig. 5. We see that the T dependence of m is reasonably well described by the power law behavior $m = m_0(1 - T/T_{\mathrm{N}})^{\beta}$. The fit over $5\ \mathrm{K} \leqslant T \leqslant T_{\mathrm{N}}$ for $T_{\mathrm{N}} = 8.25$ K as shown by the solid red curve in Fig. 5 yields a critical exponent $\beta = 0.34(4)$. This value of β is close to the value of critical exponent $\beta \approx 0.36$ expected for a three-dimensional Heisenberg system [34].

C. Muon spin relaxation

In order to further probe the magnetic ordering in $Pr_2Pd_3Ge_5$, we carried out muon spin relaxation measurements. The zero-field (ZF) asymmetry μSR spectra and their Fourier transforms for several representative temperatures are shown in Fig. 6. The occurrence of a bulk magnetic phase transition is inferred from the presence of pronounced oscillations in the asymmetry.

In the ordered state the ZF μSR asymmetry spectra are well represented by a combination of two oscillatory components having Lorentzian envelopes and one exponential term. We fitted the data using the following function:

$$G_z(t) = A_1 \cos(\omega_1 t + \phi)e^{-\lambda_1 t} + A_2 \cos(\omega_2 t + \phi)e^{-\lambda_2 t} + A_3 e^{-\lambda_3 t} + A_{\mathrm{BG}}, \tag{1}$$

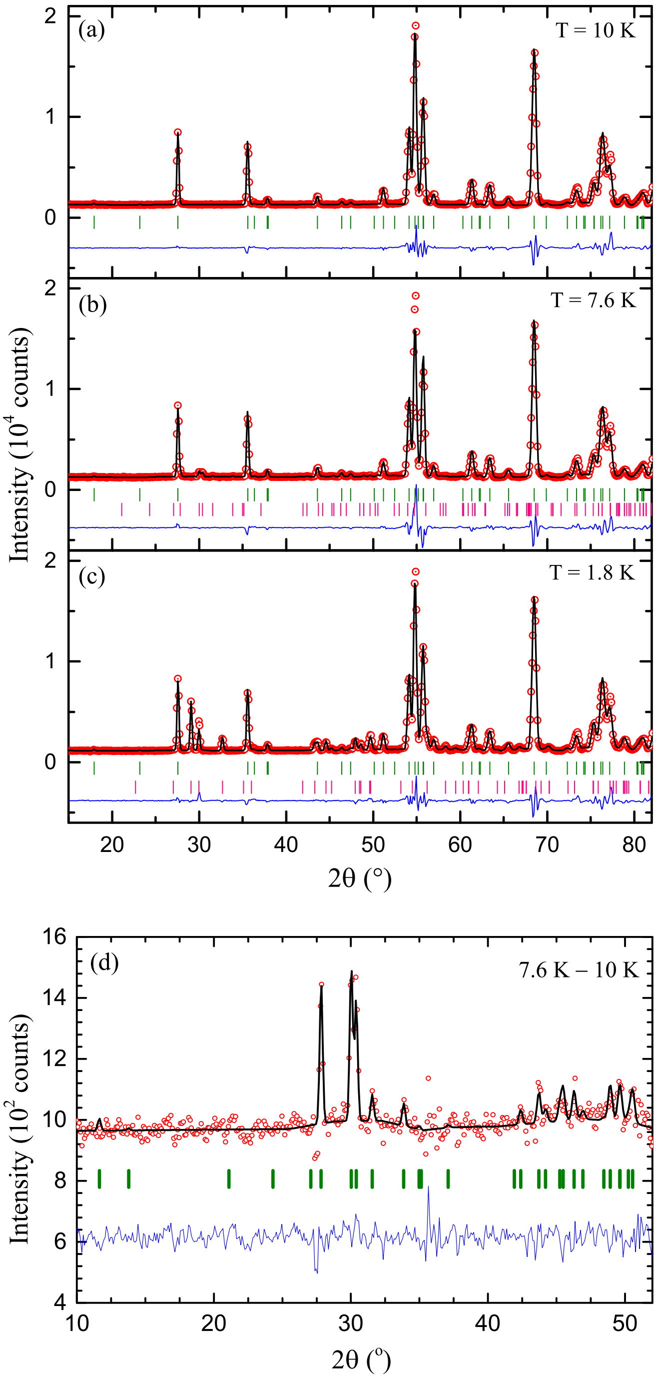

FIG. 3. (a) Neutron powder diffraction (NPD) pattern of $Pr_2Pd_3Ge_5$ recorded at 10 K together with the structural Rietveld refinement profile calculated for the $U_2Co_3Si_5$-type orthorhombic (space group *Ibam*) structure. The vertical bars indicate the nuclear Bragg peak positions. (b) The structural and magnetic refinement profile for NPD pattern at 7.6 K. (c) The structural and magnetic refinement profile for NPD pattern at 1.8 K. The lower vertical bars in (b) and (c) indicate the positions of magnetic Bragg peaks, and the upper vertical bars indicate the nuclear Bragg peak positions. (d) Magnetic diffraction pattern at 7.6 K (after subtracting the 10 K nuclear pattern) together with the calculated magnetic refinement pattern. The vertical bars indicate the positions of magnetic Bragg peaks. The lowermost blue curve in each case represents the difference between the experimental and the calculated intensities.

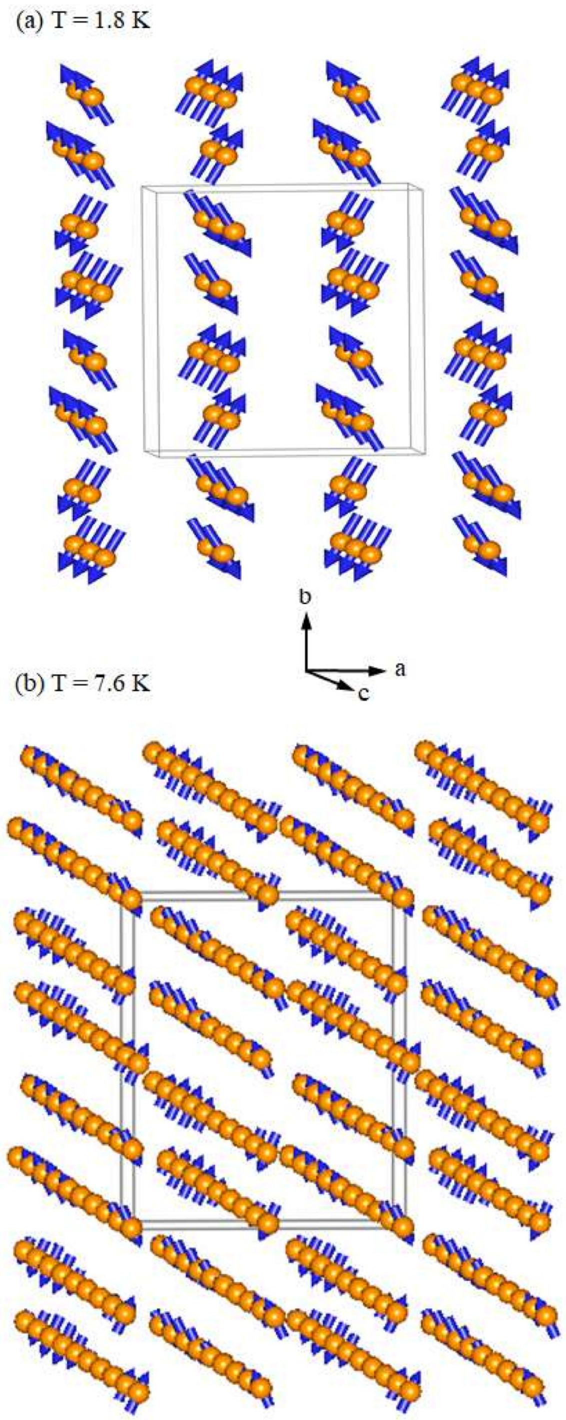

FIG. 4. Magnetic structure of $Pr_2Pd_3Ge_5$ determined from the neutron powder diffraction at (a) 1.8 K (commensurate with ordered moment 2.80(6) μ_B/Pr), and (b) 7.6 K (incommensurate sinusoidal with maximum amplitude of ordered moment 1.64 μ_B/Pr). The arrows denote the ordered Pr^{3+} magnetic moment directions.

where A_1 and A_2 are the initial asymmetries of the oscillatory components and A_3 that of the exponential term, and λ_1, λ_2 and λ_3 their relaxation rates. A_{BG} is a nonrelaxing background from sample holder, which was estimated by fitting high temperature spectra at 37 K and kept fixed while fitting the data at other temperatures. ω_1 and ω_2 are the frequencies of

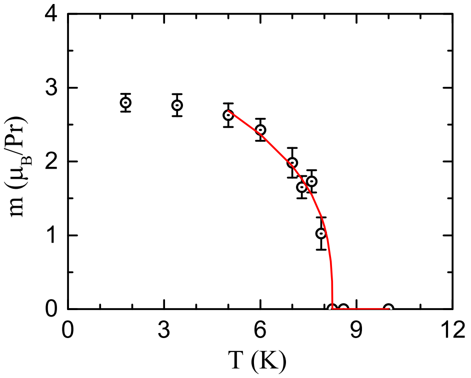

FIG. 5. Temperature T dependence of the ordered moment m determined from the neutron diffraction data of $\mathrm{Pr_2Pd_3Ge_5}$. The solid curve represents the fit over $5\ \mathrm{K} \leqslant T \leqslant T_{\mathrm{N}}$ according to $m = m_0(1 - T/T_{\mathrm{N}})^{\beta}$ for $T_{\mathrm{N}} = 8.25$ K and critical exponent $\beta = 0.34(4)$.

oscillations for the respective components, and ϕ is the phase. Oscillation frequency ω is related to the internal field B at the muon site, $\omega_1 = \gamma_\mu B_1$ and $\omega_2 = \gamma_\mu B_2$, where $\gamma_\mu = 851.615$ MHz/T is the muon gyromagnetic ratio. The representative fits to the μSR spectra at temperatures 1.5 and 6.5 K by Eq. (1) are shown by solid red curves in Figs. 6(a)–6(b). The paramagnetic state (at $T > T_{\mathrm{N1}}$) μSR spectra were fitted by removing the second term in the Eq. (1). The representative fits to the μSR spectra at temperatures 10.5 and 37 K by this modified fitting function are shown by solid red curves in Figs. 6(c)–6(d).

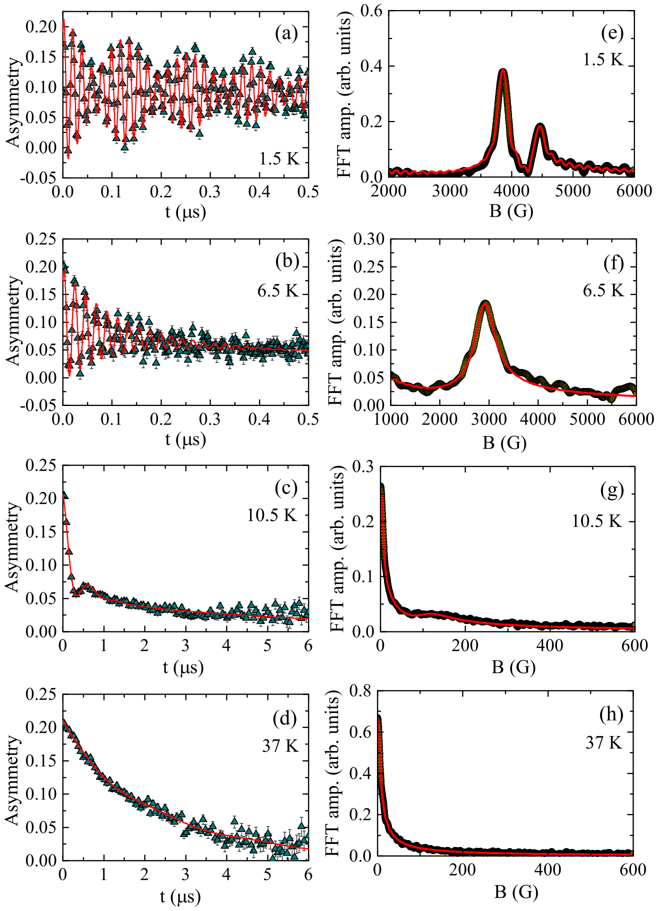

FIG. 6. (a)–(d) Zero field muon spin asymmetry function versus time t for $\mathrm{Pr_2Pd_3Ge_5}$ at few representative temperatures. (e)–(h) Fast Fourier transform (FFT) of μSR spectra, showing internal fields at the muon stopping sites. Solid curves are the fits to the μSR data by the relaxation function discussed in text.

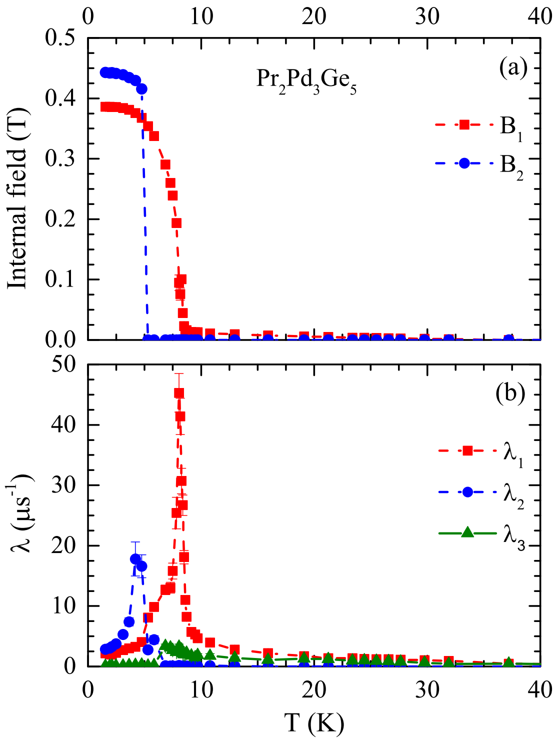

FIG. 7. Temperature T dependence of (a) internal fields B_1 and B_2, and (b) relaxation rates λ_1, λ_2, and λ_3 obtained from the fitting of the ZF-μSR spectra of $\mathrm{Pr_2Pd_3Ge_5}$ for $1.8\ \mathrm{K} \leqslant T \leqslant 37$ K.

The temperature dependence of internal fields and relaxation rates obtained from the fits of the ZF-μSR spectra by Eq. (1) (and its modified form) over the temperature range $1.5\ \mathrm{K} \leqslant T \leqslant 37$ K are presented in Fig. 7. The T dependences of B_1 and B_2 clearly mark the two transitions near 8.3 and 4.9 K, respectively [see Fig. 7(a)]. These two transitions are also clearly seen in $\lambda_1(T)$ and $\lambda_2(T)$ [Fig. 7(b)].

The appearance of peaks in the Fourier transforms shown in Figs. 6(e)-6(g) mark the long range magnetic order in $\mathrm{Pr_2Pd_3Ge_5}$. At 1.5 K two peaks are seen in fast-Fourier transform (FFT) specta [Fig. 6(e)] whereas at 6.5 K [Fig. 6(f)] only one peak is seen. We have seen very weak frequency oscillations above $T_{\mathrm{N1}} \sim 8.3$ K, see data of 10.5 K in Fig. 6(c) and the FFT in Fig. 6(g), which completely disappeared above 30 K. At present we do not have clear explanation of these weak frequency oscillations. A very similar effect has been observed in the μSR study of pyrochlores $\mathrm{Pr_2}B_2\mathrm{O_7}$ (B = Sn, Zr, Hf) and it was attributed to a hyperfine enhancement arising from a splitting of the non-Kramers doublet ground states on Pr ions close to the muon which itself causes a highly anisotropic distortion field [35]. We also calculated the muon stopping sites using the unperturbed electrostatic method (UEP), as implemented in the software

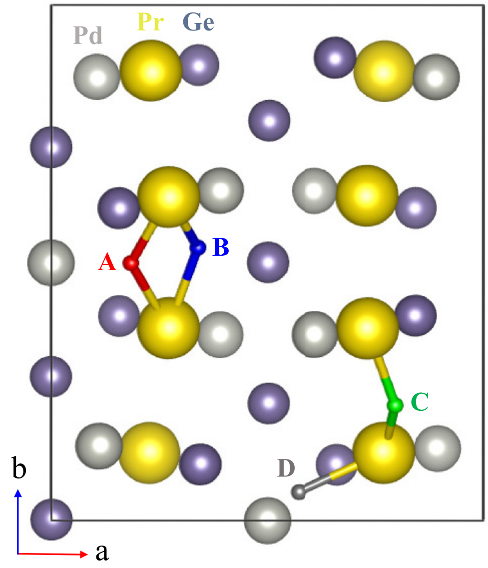

FIG. 8. Visualisation of muon stopping sites within the crystallographic unit in $Pr_2Pd_3Ge_5$. The four muon stopping sites are marked with **A**, **B**, **C**, and **D**.

package PYMUON-SUITE [36–38]. The UEP method uses density functional theory (DFT) calculations to estimate the host material's electrostatic potential, plus a combination of mathematical analysis and clustering techniques to estimate potential muon stopping sites. The DFT-based computer simulations carried out in this work were performed with the CASTEP [39] code. A plane wave cutoff of 900 eV and a k-point grid size of $3 \times 3 \times 2$ Monkhorst-Pack k point were used. The PBE exchange-correlation functional [40] was used in combination with autogenerated ultrasoft pseudopotentials. The software package PYMUON-SUITE has already shown good results for the modeling and interpretation of μSR experiments [41,42] and, in this particular case, four potential crystallographically inequivalent stopping sites were identified, which are shown in Fig. 8 marked as **A**, **B**, **C**, and **D**. These muon stopping sites correspond to the crystallographic positions **A** = (0.184, 0.5, 0.25), **B** = (0.338, 0.523, 0.197), **C** = (0.796, 0.223, 0.306), and **D** = (0.573, 0.055, 0).

We estimated the internal fields at these muon stopping sites using the dipolar contribution calculated using the DIPOLECALC program [43]. For the commensurate structure at 1.8 K we took a moment of 2.8 μ_B and for the incommensurate structure at 7.5 K we estimated the maximum field taking the moment to have the uniform value 1.64 μ_B. This uniform approximation provides a good estimate of the maximum field because the modulation period is long and the dipolar field for an AF state is dominated by the closest moments to the probe site. Since the field distribution taking into account the modulation is strongly peaked at the maximum field (inset to Fig. 9), these maximum fields are the ones that should be compared with the peaks in the FFT spectra. The dipolar field distribution of muon stopping sites is shown in Fig. 9. Note that site **D** is on a symmetry plane and has lower multiplicity than the other three sites. The estimated values of dipolar fields at different muon stopping sites are listed in Table II. As seen from Fig. 6(e), at 1.5 K the FFT spectra exhibit two peaks near 3.8 and 4.5 kG, which are close to the dipolar fields at sites **D** (3.427 kG) and **B** (4.359 kG), respectively. The values of internal fields B_1 and B_2 obtained from μSR analysis are 3.860 and 4.427 kG, respectively [Fig. 7(a)]. At 7.5–7.6 K the FFT spectra show peaks near 2.4 kG and 2.1 kG, which are again close to the maximum dipolar fields at sites **D** (2.448 kG) and **B** (1.777 kG), respectively. Thus, we conclude that the muons are mainly stopping at the **D** site, but some also stop at the **B** site. The **B** site gives the weaker satellite signals, which switch

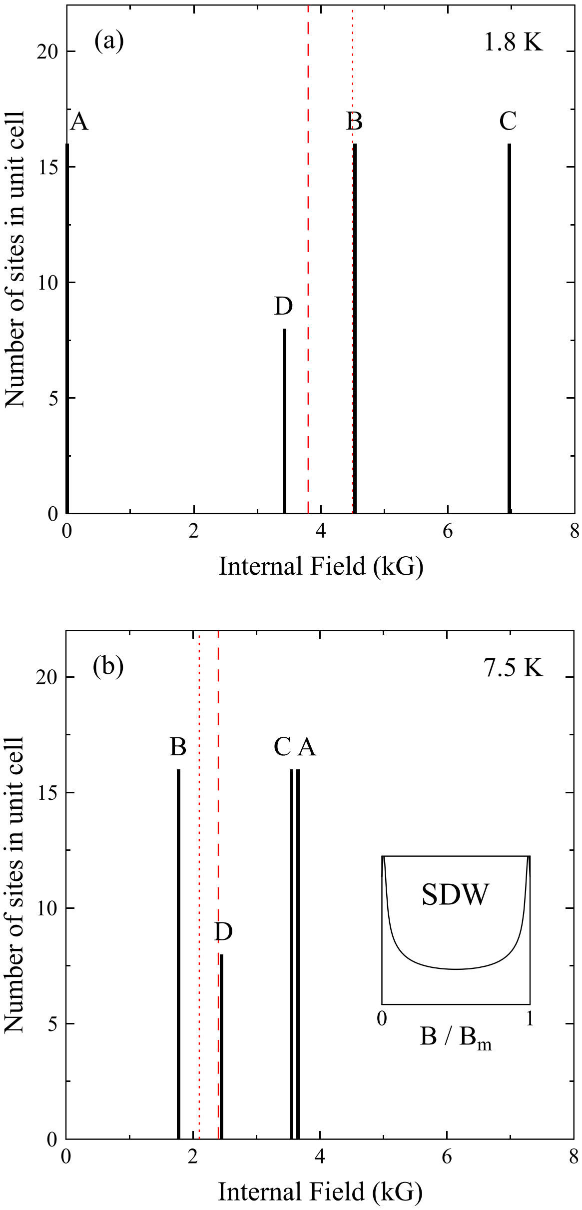

FIG. 9. Dipolar field distribution at muon stopping sites **A**, **B**, **C**, and **D** in $Pr_2Pd_3Ge_5$ for (a) the low-T commensurate structure and (b) the high-T incommensurate SDW structure. The vertical red dashed and dotted lines represent the values of the internal magnetic fields estimated from the dominant features in the experimental data illustrated in Figs. 6 and 7 and listed in the final row of Table II. In (b) the field distribution in the SDW phase corresponding to each type of site is strongly peaked at zero field and the maximum field (inset), so only the maximum field values are shown in the main plot for making comparison with the FFT peaks.

TABLE II. Estimated values of dipolar fields at different muon stopping sites of $Pr_2Pd_3Ge_5$ along with the values obtained from FFT spectra. The dipolar field values at higher temperature are the maximum values within the incommensurate structure.

	1.8 K		7.5–7.6 K	
Sites	kG	kG/μ_B	kG	kG/μ_B
A	0.005	0.002	3.652	2.23
B	4.539	1.64	1.777	1.08
C	6.967	2.49	3.553	2.17
D	3.427	1.16	2.448	1.49
FFT spectra	3.8, 4.5		2.4, 2.1	

from the high field side in the low-T (1.5 K) phase to the low field side in the high-T (7.5 K) phase (see Fig. 9).

D. Inelastic neutron scattering

The inelastic neutron scattering responses from $Pr_2Pd_3Ge_5$ and $La_2Rh_3Ge_5$ measured with an incident energy $E_i =$ 20 meV at $T = 5$ K are shown in Figs. 10(a) and 10(b) as the color coded intensity maps. The data of $Pr_2Pd_3Ge_5$ at 10 K are given in Fig. 12(d) of the Appendix. Further, the INS responses from $Pr_2Pd_3Ge_5$ and $La_2Rh_3Ge_5$ measured with $E_i = 6$ meV at $T = 5$ K are shown in Figs. 12(a) and 12(b), respectively and at 10 K from $Pr_2Pd_3Ge_5$ is shown in Fig. 12(c). The estimated magnetic scattering from $Pr_2Pd_3Ge_5$ at 5 K and 10 K with $E_i = 20$ meV is given in Figs. 10(c) and 10(d). The excitations of magnetic origin are evident from the color contour maps of $Pr_2Pd_3Ge_5$ when comparing with that of the nonmagnetic reference $La_2Rh_3Ge_5$. The INS map of $Pr_2Pd_3Ge_5$ with $E_i = 6$ meV at 5 K [Fig. 12(a)] reveals a weak excitation near 1.7 meV, which is not present at 10 K and also not observed in $La_2Rh_3Ge_5$ at 5 K. This excitation was also observed at 3.8 K, but not at 9.1 K in the 4F1 triple axis spectrometer measurements at LLB (data not shown). As $T_{N1} \sim 8.3$ K, this low energy excitation at 5 K in $Pr_2Pd_3Ge_5$ originates from the powder average spin waves in the magnetic ordered state. The INS map of $Pr_2Pd_3Ge_5$ with $E_i = 20$ meV at 5 K reveals four excitations, 1.7, 8.3, 9.2, and 12.8 meV [Fig. 10(c)] and additional excitation near 18.6 meV was observed in the E_i=30 meV data Figs. 13(a) and 13(c). The separation between 8.3 and 9.2 meV excitations is reduced and they move slightly to lower energies (i.e., at 7.7 and 8.3 meV) at 10 K Figs. 10(c) and 10(d), which indicates that the Zeeman spliting of the CEF level under the molecular field in the magnetic order state gives two well-resolved excitations at 5 K.

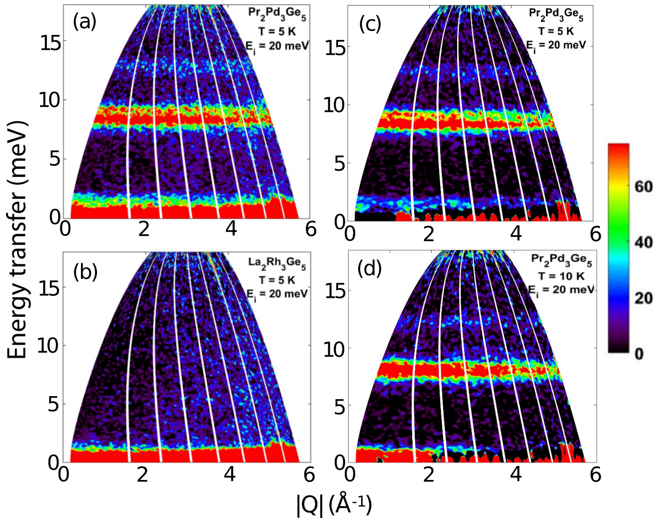

FIG. 10. Inelastic neutron scattering response, a color-coded contour map of the intensity, energy transfer E versus momentum transfer $|Q|$ for (a) $Pr_2Pd_3Ge_5$ and (b) $La_2Rh_3Ge_5$ measured at 5 K with an incident energy $E_i = 20$ meV. (c), (d) The estimated magnetic scattering after subtracting the phonon scattering at 5 K and 10 K for $Pr_2Pd_3Ge_5$.

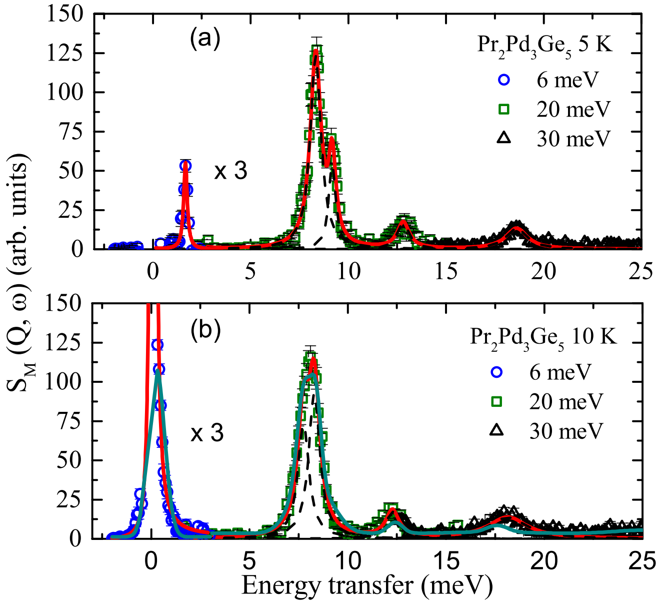

FIG. 11. The estimated Q integrated ($Q = 0$ to 3 Å^{-1}) magnetic scattering intensity plotted as, energy transfer E versus $S_M(|Q|, \omega)$ for $Pr_2Pd_3Ge_5$ (a) at 5 K and (b) at 10 K. The results are combined for three different incident energies, $E_i = 6$, 20, and 30 meV. The solid red line shows the fit using Lorentzian functions and dotted lines show the components of the fit. The solid light green line in (b) shows the fit based on the CEF model.

The magnetic scattering $S_M(Q, \omega)$ is obtained by subtracting the phonon background using the INS data of $La_2Rh_3Ge_5$ as $S_M(Q, \omega) = S(Q, \omega)_{Pr_2Pd_3Ge_5} - \alpha S(Q, \omega)_{La_2Rh_3Ge_5}$ where $\alpha = 0.8114$ is the ratio of total bound neutron scattering cross sections per formula unit of $Pr_2Pd_3Ge_5$ and $La_2Rh_3Ge_5$. The one-dimensional energy cuts from the magnetic scattering, $S_M(Q, \omega)$, for $Pr_2Pd_3Ge_5$ at 5 K and 10 K are shown in Figs. 11(a) and 11(b). These data show that in the paramagnetic state (at 10 K) we have observed four CEF excitations, 7.7, 8.3, 12.3, and 18.1 meV, see Fig. 11(b). In the orthorhombic crystal structure, space group *Ibam* (No. 72), of $Pr_2Pd_3Ge_5$, the Pr ions occupy the $8j$ crystallographic site having point symmetry C_s (monoclinic). Hence the CEF Hamiltonin (H_{CEF}) has following form:

$$\begin{aligned} H_{CEF} = {} & B_2^0 O_2^0 + B_2^{\pm 2} O_2^{\pm 2} + B_4^0 O_4^0 + B_4^{\pm 2} O_4^{\pm 2} + B_4^{\pm 4} O_4^{\pm 4} \\ & + B_6^0 O_6^0 + B_6^{\pm 2} O_6^{\pm 2} + B_6^{\pm 4} O_6^{\pm 4} + B_6^{\pm 6} O_6^{\pm 6}, \end{aligned} \tag{2}$$

TABLE III. Crystal electric field parameters $B_n^{\pm m}$ obtained from the analysis of the inelastic neutron scattering data of $Pr_2Pd_3Ge_5$ at 10 K.

$B_n^{\pm m}$	Value (*meV*)
B_2^{-2}	0.2115
B_2^0	−0.4372
B_2^2	0.0189
B_4^{-4}	−0.0188
B_4^{-2}	−0.0116
B_4^0	5.245×10^{-4}
B_4^2	7.806×10^{-3}
B_4^4	-4.305×10^{-3}
B_6^{-6}	-8.410×10^{-5}
B_6^{-4}	-9.652×10^{-6}
B_6^{-2}	-1.042×10^{-4}
B_6^0	-6.690×10^{-6}
B_6^2	6.079×10^{-5}
B_6^4	6.362×10^{-5}
B_6^6	4.984×10^{-5}

where $B_n^{\pm m}$ are the CEF parameters and need to be determined from the fitting of the experimental data such as CEF excitations measured using INS or resonance x-ray scattering (RIXS) and/or single-crystal susceptibility. $O_n^{\pm m}$ are Stevens operators [44] and are functions of angular momentum operators $O_n^{\pm m} = O_n^{\pm m}(J)$. Due to the low point symmetry of the Pr ions we have nonzero contribution to CEF parameters with $B_n^{\pm m}$ (i.e., with negative value of $-m$). The $O_n^{\pm m}$ with $+m$ are real terms (sometimes called "cosine" terms) and with $-m$ are the imaginary terms (sometimes called "sine" terms). The ground state multiplet of Pr^{3+} ion with $J = 4$ will split into nine singlets under the crystal field potential given in Eq. (2). The H_{CEF} given in Eq. (2) has 15 independent CEF parameters to be determined from the analysis of the experimental data. As we have observed four CEF excitations from the ground state at 10 K, it would be very difficult to uniquely determine the 15 CEF parameters. Hence, we use a point charge model to estimate the initial set of CEF parameters that gave the calculated CEF excitations very close the observed one. This set of estimated CEF parameters was then used to fit the INS data at 10 K using MANTIDPLOT [45]. The parameters obtained from the fit are given in Table III. The calculated CEF spectra using this set of CEF parameters gave very strong excitations near 7.8 and 8.6 meV and other weak excitations near 12.4, 17.5, and 25.2 meV [see fit given in Fig. 11(b)]. The calculated spectrum is very close to the observed data.

The scheme of the CEF levels obtained from the CEF analysis of INS data is: 0, 0.27, 7.78, 8.66, 12.42 17.45, 17.61, 25.24, and 25.39 meV. The CEF wave functions associated with these nine energy levels are listed in Table IV. The two singlets at 0 and 0.3 meV together form a quasidoublet ground state, as also inferred from the $S_{mag}(T)$. The estimated ordered state moment (in an applied field of 5 T) from the ground state wave functions are $\mu_x = 0.08\ \mu_B$, $\mu_y = 0.15\ \mu_B$, and $\mu_z = 3.05\ \mu_B$. The CEF model shows the easy axis of the magnetization to be the z axis (i.e., along c axis), which is also in agreement with the single crystal susceptibility results [23]. The magnitude of the estimated CEF moment is in close agreement with that estimated from the neutron diffraction study, however, there is a disagreement between the direction of the moment obtained from the neutron diffraction study and the CEF analysis. Considering this we checked again the neutron diffraction data forcing the moment direction along the c axis. However, the so simulated diffraction patterns did not at all correspond to the observed magnetic Bragg peaks. We therefore believe that the direction of the moment is not only controlled by the single ion CEF anisotropy, but also by the anisotropic two ion exchange interactions. A very similar situation is observed for the hard axis ordering in many Ce-based compounds [46], for example in $CeRu_2Al_{10}$ [47] and $CeOs_2Al_{10}$ [48]. Furthermore, a theoretical model has been also presented based on the fluctuation-driven hard-axis magnetic ordering in metallic ferromagnets [49]. Thus further theoretical and experimental works are sought to fully understand the observed hard axis ordering in $Pr_2Pd_3Ge_5$.

IV. SUMMARY AND CONCLUSIONS

The magnetism and crystal field states of $Pr_2Pd_3Ge_5$ have been investigated by muon spin relaxation, neutron powder diffration, and inelastic neutron scattering measurements. Our $\chi'(T)$ and $C_p(T)$ data confirmed the occurrence of two antiferromagnetic transitions at $T_{N1} = 8.25$ K and $T_{N2} = 7.5$ K as found previously for polycrystalline $Pr_2Pd_3Ge_5$ [22]. The appearance of magnetic Bragg peaks in neutron diffraction data collected at $T < T_{N1}$ further confirms the long-range antiferromagnetic ordering in this compound. The magnetic Bragg peaks could be indexed with the propagation vector $\mathbf{k} = (1, 0, 0)$ for $T < T_{N2}$, and with $\mathbf{k} = (1, 0, 0.070(1))$ for $T_{N2} < T < T_{N1}$. The magnetic structure determined by the refinement of NPD data revealed a canted antiferromagnetic structure of ordered Pr^{3+} moments. Given the resolution of neutron powder diffraction our NPD data reveal the presence of only two magnetic structures associated with antiferromagnetic transitions at T_{N1} and T_{N2}. At 7.6 K, which lies between T_{N2} and T_{N1}, the magnetic structure refinement reveals an amplitude modulated incommensurate antiferromagnetic arrangement of ordered moments. The ordered moments lie in the ab plane tilted at about 26° from the b axis and have a maximum ordered moment of 1.64(3) μ_B/Pr. On the other hand, at T below T_{N2}, i.e., at 1.8 K, the NPD data reveal a commensurate antiferromagnetic structure with an ordered moment of 2.80(6) μ_B/Pr. The ordered Pr moments lie still in the ab plane with only a slightly different tilt angle of about 28° from the b axis.

The μSR data also provide evidence for the bulk magnetic phase transitions. The presence of two oscillatory frequencies in the μSR spectra at 1.5 K clearly attests to the occurrence of long range magnetic order in $Pr_2Pd_3Ge_5$. The T dependence of fit parameters reflects two magnetic phase transitions near 8.3 and 4.9 K. The observed internal fields can be well explained by the calculated internal fields, using a dipolar model, at the muon stopping sites estimated from the DFT calculation. The inelastic neutron scattering data show four CEF excitations arising from the CEF splitting of the Pr^{3+} $J = 4$ ground state multiplet and the CEF-level scheme has been obtained from the analysis of the INS data based on the CEF model. The CEF model analysis reveals a quasi-

TABLE IV. Energy levels and associated wave functions obtained from the analysis of inelastic neutron scattering data of $Pr_2Pd_3Ge_5$ at 10 K by a model based on crystal electric field.

Energy levels (meV)	Wave functions
0	$0.688\,\lvert -4\rangle - (0.099 + i\,0.075)\,\lvert -2\rangle + (0.021 - i\,0.152)\lvert 0\rangle + (0.115 - i\,0.045)\lvert 2\rangle - (0.661 + i\,0.189)\lvert 4\rangle$
0.27	$-0.688\,\lvert -4\rangle + (0.121 + i\,0.107)\,\lvert -2\rangle - (0.016 + i\,0.002)\,\lvert 0\rangle + (0.147 - i\,0.068)\,\lvert 2\rangle - (0.660 + i\,0.196)\,\lvert 4\rangle$
7.78	$(0.030 - i\,0.654)\,\lvert -3\rangle + (0.120 + i\,0.238)\,\lvert -1\rangle - (0.266 + i\,0.023)\,\lvert 1\rangle + (0.596 - i\,0.270)\,\lvert 3\rangle$
8.66	$(0.235 - i\,0.659)\,\lvert -3\rangle - (0.041 + i\,0.095)\,\lvert -1\rangle - (0.082 + i\,0.062)\,\lvert 1\rangle - (0.696 - i\,0.069)\,\lvert 3\rangle$
12.42	$0.167\,\lvert -4\rangle + (0.564 + i\,0.359)\,\lvert -2\rangle - (0.218 - i\,0.045)\,\lvert 0\rangle + (0.374 - i\,0.555)\,\lvert 2\rangle + (0.153 - i\,0.067)\,\lvert 4\rangle$
17.45	$-0.158\,\lvert -4\rangle - (0.414 + i\,0.428)\,\lvert -2\rangle - (0.056 +\ 0.487)\,\lvert 0\rangle + (0.307 - i\,0.511)\,\lvert 2\rangle + (0.154 - i\,0.036)\,\lvert 4\rangle$
17.61	$-(0.160 + i\,0.186)\,\lvert -3\rangle - (0.262 + i\,0.609)\,\lvert -1\rangle + (0.417 - i\,0.516)\,\lvert 1\rangle + (0.204 - i\,0.136)\,\lvert 3\rangle$
25.24	$(0.126 + i\,0.077)\,\lvert -3\rangle - (0.022 + i\,0.691)\,\lvert -1\rangle - (0.634 - i\,0.276)\,\lvert 1\rangle + (0.123 + i\,0.081)\,\lvert 3\rangle$
25.39	$-0.023\,\lvert -4\rangle + (0.378 + i\,0.117)\,\lvert -2\rangle - (0.095 + i\,0.823)\lvert 0\rangle - (0.341 - i\,0.200)\,\lvert 2\rangle + (0.022 - i\,0.005)\,\lvert 4\rangle$

doublet (two closely situated singlets separated in energy by 0.3 meV) ground state which is consistent with the magnetic entropy data.

ACKNOWLEDGMENTS

We thank J.-M. Mignot for his experimental assistance on 4F1 triple axis spectrometer at LLB. We thank C. Geibel for fruitful discussions. V.K.A. and D.T.A. acknowledge financial assistance from CMPC-STFC Grant No. CMPC-09108. D.T.A. thanks EPSRC UK for the funding (Grant Ref: No. EP/W00562X/1) and the Royal Society of London for the Newton Advanced Fellowship between UK and China and International Exchange funding between UK and Japan. A.B. would like to acknowledge financial support from the Department of Science and Technology, India (SR/NM/Z-07/2015) and Jawaharlal Nehru Centre for Advanced Scientific Research (JNCASR), and the Science & Engineering Research Board for the CRG Research Grant (CRG/2020/000698). Z.H. acknowledges support from Department of Science and Technology (India). We thank the ISIS Facility for the beam time RB1120392 (the INS data are available at Ref. [50]), and RB1220471 (the INS data are available at Ref. [51]).

APPENDIX: INELASTIC NEUTRON SCATTERING DATA FOR $E_i = 6, 20, 30$ meV

Figures 12 and 13 show the color coded intensity maps of $Pr_2Pd_3Ge_5$ and $La_2Rh_3Ge_5$ measured at 5 and 10 K with $E_i =$ 6 meV, 20 meV, 30 meV, and 40 meV as labeled.

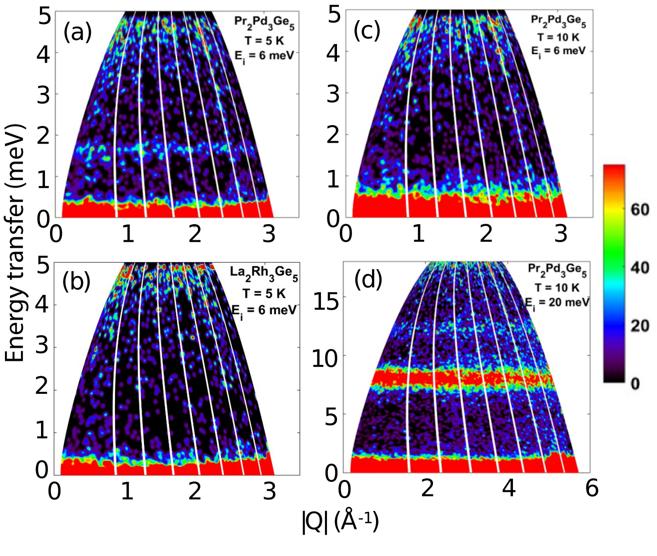

FIG. 12. Inelastic neutron scattering (INS) response, a color-coded contour map of the intensity, energy transfer E versus momentum transfer $|Q|$ for (a) $Pr_2Pd_3Ge_5$ measured at 5 K with an incident energy $E_i = 6$ meV, (b) $La_2Rh_3Ge_5$ at 5 K ($E_i = 6$ meV), (c) $Pr_2Pd_3Ge_5$ at 10 K ($E_i = 6$ meV), (d) $Pr_2Pd_3Ge_5$ at 10 K ($E_i =$ 20 meV).

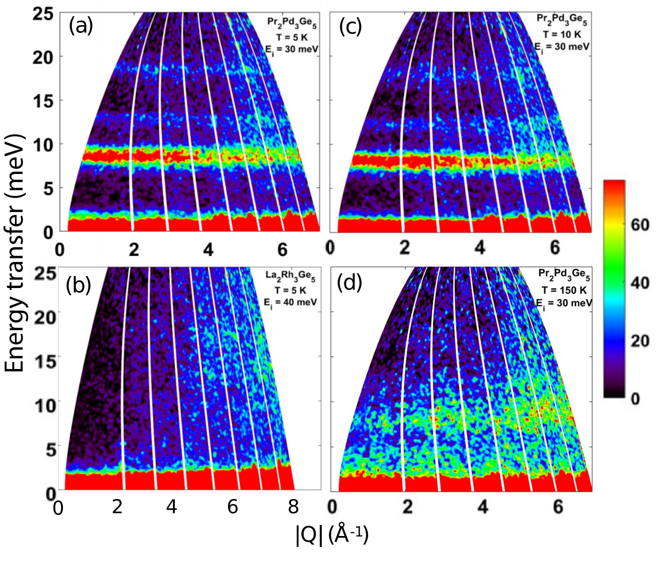

FIG. 13. Inelastic neutron scattering (INS) response, a color-coded contour map of the intensity, energy transfer E versus momentum transfer $|Q|$ for (a) $Pr_2Pd_3Ge_5$ measured at 5 K with an incident energy $E_i = 30$ meV, (b) $La_2Rh_3Ge_5$ at 5 K ($E_i = 40$ meV), (c) $Pr_2Pd_3Ge_5$ at 10 K ($E_i = 30$ meV). (d) $Pr_2Pd_3Ge_5$ at 150 K ($E_i = 30$ meV).

[1] G. T. Trammell, Phys. Rev. **131**, 932 (1963).
[2] B. R. Cooper, Phys. Rev. **163**, 444 (1967).
[3] Y. L. Wang and B. R. Cooper, Phys. Rev. **172**, 539 (1968).
[4] R. J. Birgeneau, J. Als-Nielsen, and E. Bucher, Phys. Rev. Lett. **27**, 1530 (1971).
[5] K. Andres, E. Bucher, S. Darack, and J. P. Maita, Phys. Rev. B **6**, 2716 (1972).
[6] A. F. Deutz, H. B. Brom, H. Deelen, L. J. de Jongh and W. J. Huiskamp, and K. H. J. Buschow, Solid State Commun. **60**, 917 (1986).
[7] A. F. Deutz, H. B. Brom, C. D. Wentworth, W. J. Huiskamp, L. J. de Jongh, and K. H. J. Buschow, J. Magn. Magn. Mater. **78**, 176 (1989).
[8] E. A. Goremychkin, I. Natkaniec, E. Mühle, and O. D. Chistyakov, J. Magn. Magn. Mater. **81**, 63 (1989).
[9] A. D. Christianson and J. M. Lawrence, J. L. Zarestky, H. S. Suzuki, J. D. Thompson, M. F. Hundley, J. L. Sarrao, C. H. Booth, D. Antonio, and A. L. Cornelius, Phys. Rev. B **72**, 024402 (2005).
[10] A. D. Christianson, J. M. Lawrence, K. C. Littrell, E. A. Goremychkin, A. I. Kolesnikov, J. D. Thompson, and J. L. Sarrao, J. Appl. Phys. **101**, 09D505 (2007).
[11] A. M. Mulders, A. Yaouanc, P. Dalmas de Réotier, P. C. M. Gubbens, A. A. Moolenaar, B. Fåk, E. Ressouche, K. Prokeš, A. A. Menovsky, and K. H. J. Buschow, Phys. Rev. B **56**, 8752 (1997).
[12] V. K. Anand, D. T. Adroja, A. Bhattacharyya, A. D. Hillier, J. W. Taylor, and A. M. Strydom, J. Phys.: Condens. Matter **26**, 306001 (2014).
[13] V. K. Anand, D. T. Adroja, and A. D. Hillier, J. Phys.: Condens. Matter **25**, 196003 (2013).
[14] A. Krimmel, J. Hemberger, M. Nicklas, G. Knebel, W. Trinkl, M. Brando, V. Fritsch, A. Loidl, and E. Ressouche, Phys. Rev. B **59**, R6604 (1999).
[15] E. A. Goremychkin, R. Osborn, B. D. Rainford, R. T. Macaluso, D. T. Adroja, and M. Koza, Nat. Phys. **4**, 766 (2008).
[16] V. K. Anand, D. T. Adroja, A. D. Hillier, and J. Taylor, G. Andre, Phys. Rev. B **84**, 064440 (2011).
[17] V. K. Anand, D. T. Adroja, and A. D. Hillier, Phys. Rev. B **85**, 014418 (2012).
[18] V. K. Anand Anupam, Z. Hossain, D. T. Adroja, and C. Geibel, J. Phys.: Condens. Matter **23**, 376001 (2011).
[19] E. D. Bauer, N. A. Frederick, P. C. Ho, V. S. Zapf, and M. B. Maple, Phys. Rev. B **65**, 100506(R) (2002).
[20] E. A. Goremychkin, R. Osborn, E. D. Bauer, M. B. Maple, N. A. Frederick, W. M. Yuhasz, F. M. Woodward, and J. W. Lynn, Phys. Rev. Lett. **93**, 157003 (2004).
[21] V. K. Anand, Z. Hossain, G. Chen, M. Nicklas, and C. Geibel, Phys. Rev. B **79**, 113107 (2009).
[22] V. K. Anand, Z. Hossain, and C. Geibel, Phys. Rev. B **77**, 184407 (2008).
[23] V. K. Anand, A. Thamizhavel, Z. Hossain, and S. Ramakrishnan, J. Phys.: Condens. Matter **24**, 456003 (2012).
[24] Anupam, V. K. Anand, V. Ganesan, and Z. Hossain, J. Magn. Magn. Mater. **321**, 2753 (2009).
[25] S. Layek, V. K. Anand, and Z. Hossain, J. Magn. Magn. Mater. **321**, 3447 (2009).
[26] V. K. Anand, A. K. Nandy, S. K. Dhar, C. Geibel, and Z. Hossain, J. Magn. Magn. Mater. **313**, 164 (2007).
[27] V. K. Anand, Anupam, Z. Hossain, S. Ramakrishnan, A. Thamizhavel, and D. T. Adroja, J. Magn. Magn. Mater. **324**, 2483 (2012).
[28] A. Suter and B. M. Wojek, Phys. Procedia **30**, 69 (2012).
[29] J. Rodríguez-Carvajal, Physica B: Condens. Matter **192**, 55 (1993); Program Fullprof, LLB-JRC, Laboratoire Léon Brillouin, CEA-Saclay, France, 1996 (www.ill.eu/sites/fullprof/).
[30] L. Durivault, F. Bourée, B. Chevalier, G. André, and J. Etourneau, J. Magn. Magn. Mater. **246**, 366 (2002).
[31] F. Honda, N. Metoki, T. D. Matsuda, Y. Haga, A. Thamizhavel, Y. Okuda, R. Settai, and Y. Onuki, J. Alloys Compd. **451**, 504 (2008).
[32] J. Rodriguez-Carvajal, BASIREPS: A program for calculating irreducible representations of space groups and basis functions for axial and polar vector properties. Part of the FULLPROF Suite of programs (www.ill.eu/sites/fullprof/).
[33] C. Ritter, Solid State Phenom. **170**, 263 (2011).
[34] S. Blundell, *Magnetism in Condensed Matter* (Oxford University Press, New York, 2001).
[35] F. R. Foronda, F. Lang, J. S. Möller, T. Lancaster, A. T. Boothroyd, F. L. Pratt, S. R. Giblin, D. Prabhakaran, and S. J. Blundell, Phys. Rev. Lett. **114**, 017602 (2015)
[36] S. Sturniolo and L. Liborio, J. Chem. Phys. **153**, 044111 (2020).
[37] L. Liborio, S. Sturniolo, and D. Jochym, J. Chem. Phys. **148**, 134114 (2018).
[38] S. Sturniolo, L. Liborio, and S. Jackson, J. Chem. Phys. **150**, 154301 (2019).
[39] S. J. Clark, M. D. Segall, C. J. Pickard, P. J. Hasnip, M. I. J. Probert, K. Refson, and M. C. Payne, Z. Kristallogr. - Cryst. Mater. **220**, 567 (2005).
[40] J. P. Perdew, K. Burke, and M. Ernzerhof, Phys. Rev. Lett. **77**, 3865 (1996).
[41] C. Mielke III, W. Ma, V. Pomjakushin, O. Zaharko, S. Sturniolo, X. Liu, V. Ukleev, J. S. White, J.-X. Yin, S. S. Tsirkin, C. B. Larsen, T. A. Cochran, M. Medarde, V. Porée, D. Das, R. Gupta, C. N. Wang, J. Chang, Z. Q. Wang, R. Khasanov, T. Neupert, A. Amato, L. Liborio, S. Jia, M. Z. Hasan, H. Luetkens, and Z. Guguchia, Commun. Phys. **5**, 107 (2022).
[42] C. Yue, L. Liborio, T. Bian, S. Sturniolo, J. Wright, S. P. Cottrell, R. Khasanov, G. Simutis, U. A. Jayasooriya, and Y. Chao, J. Phys. Chem. C **124**, 9656 (2020).
[43] F. L. Pratt, Dipolar Field Calculations for Muon Spectroscopy (2019), https://doi.org/10.5281/zenodo.3476167.
[44] K. W. H. Stevens, Proc. Phys. Soc. London A **65**, 209 (1952).
[45] O. Arnold, J. C. Bilheux, J. M. Borreguero, A. Buts, S. I. Campbell, L. Chapon, M. Doucet, N. Draper, R. Ferraz Leal, M. A. Gigg, V. E. Lynch, A. Markvardsen, D. J. Mikkelson, R. L. Mikkelson, R. Miller, K. Palmen, P. Parker, G. Passos, T. G. Perring, P. F. Peterson, S. Ren, M. A. Reuter, A. T. Savici, J. W. Taylor, R. J. Taylor, R. Tolchenov, W. Zhou, and J. Zikovsky, Nucl. Instrum. Methods Phys. Res., Sect. A **764**, 156 (2014).
[46] M. Brando, D. Belitz, F. M. Grosche, and T. R. Kirkpatrick, Rev. Mod. Phys. **88**, 025006 (2016).
[47] D. D. Khalyavin, A. D. Hillier, D. T. Adroja, A. M. Strydom, P. Manuel, L. C. Chapon, P. Peratheepan, K. Knight, P. Deen,

C. Ritter, Y. Muro, and T. Takabatake, Phys. Rev. B **82**, 100405(R) (2010).

[48] H. Kato, R. Kobayashi, T. Takesaka, T. Nishioka, M. Matsumura, K. Kaneko, and N. Metoki, J. Phys. Soc. Jpn. **80**, 073701 (2011).

[49] F. Krüger, C. J. Pedder, and A. G. Green, Phys. Rev. Lett. **113**, 147001 (2014)

[50] https://doi.org/10.5286/ISIS.E.24088147.

[51] https://doi.org/10.5286/ISIS.E.24089711.